Communications in Theoretical Physics

Commun. Theor. Phys. **77** (2025) 085401 (13pp) https://doi.org/10.1088/1572-9494/adb5f5
CSTR: 32041.14.CTP.adb5f5

Constraints on typical relic gravitational waves based on data of LIGO

Minghui Zhang and Hao Wen*

Department of Physics, Chongqing Key Laboratory for Strongly Coupled Physics, Chongqing University, Chongqing 401331, China

E-mail: wenhao@cqu.edu.cn

Received 28 March 2024, revised 18 January 2025
Accepted for publication 24 January 2025
Published 11 April 2025

Abstract

Relic gravitational waves (RGWs) from the early Universe carry crucial and fundamental cosmological information. Therefore, it is of extraordinary importance to investigate potential RGW signals in the data from observatories such as the LIGO-Virgo-KAGRA network. Here, focusing on typical RGWs from the inflation and the first-order phase transition (by sound waves and bubble collisions), effective and targeted deep learning neural networks are established to search for these RGW signals within the real LIGO data (O2, O3a and O3b). Through adjustment and adaptation processes, we develop suitable Convolutional Neural Networks (CNNs) to estimate the likelihood (characterized by quantitative values and distributions) that the focused RGW signals are present in the LIGO data. We find that if the constructed CNN properly estimates the parameters of the RGWs, it can determine with high accuracy (approximately 94% to 99%) whether the samples contain such RGW signals; otherwise, the likelihood provided by the CNN cannot be considered reliable. After testing a large amount of LIGO data, the findings show no evidence of RGWs from: 1) inflation, 2) sound waves, or 3) bubble collisions, as predicted by the focused theories. The results also provide upper limits of their GW spectral energy densities of $h^2\Omega_{\rm gw} \sim 10^{-5}$, respectively for parameter boundaries within 1) [$\beta \in (-1.87, -1.85) \times \alpha \in (0.005, 0.007)$], 2) [$\beta/H_{\rm pt} \in (0.02, 0.16) \times \alpha \in (1, 10) \times T_{\rm pt} \in (5{*}10^9, 10^{10})$ Gev], and 3) [$\beta/H_{\rm pt} \in (0.08, 0.2) \times \alpha \in (1, 10) \times T_{\rm pt} \in (5 * 10^9, 8 * 10^{10})$ Gev]. In short, null results and upper limits are obtained, and the analysis suggests that our developed methods and neural networks to search for typical RGWs in the LIGO data are effective and reliable, providing a viable scheme for exploring possible RGWs from the early Universe and placing constraints on relevant cosmological theories.

Keywords: relic gravitational wave, early Universe, LIGO, deep learning neural networks

(Some figures may appear in colour only in the online journal)

1. Introduction

In recent years, multiple gravitational wave (GW) signals from compact binary coalescences (CBCs) have been captured by the network of the LIGO-Virgo-KAGRA collaboration [1–4], marking a groundbreaking discovery that has rapidly brought us into the age of GW astronomy. Meanwhile, the stochastic gravitational wave background (SGWB) arises as a superposition of unresolved and uncorrelated GW signals from various origins [5, 6], including astrophysical sources such as CBCs [7–9], neutron stars (NSs) [10–12], core collapses [13–18], or cosmological sources such as cosmic strings [19–25], phase transition [26–28], inflation [29–32], primordial black holes [33] and domain walls [34]. The SGWB contains GWs with a spectrum that spans a very wide frequency range and carries extremely rich and crucial information about fundamental questions of the Universe, so this is an urgent and widely focused experimental target of GW detections. If certain components of the SGWB fall within the sensitivity and frequency range of LIGO, it is anticipated that the recorded data would encompass signals and traces of these GWs. However, identifying or searching

* Author to whom any correspondence should be addressed.

Table 1. The structure of the CNN used to calculate the confidence of the presence of typical GW signals in the real LIGO data.

Layer type	Channel	Kernel size
Input		
Conv1D+Relu	8	4
MaxPool1D		4
Conv1D+Relu	16	8
MaxPool1D		3
Conv1D+Relu	32	3
MaxPool1D		2
Flatten		
Dropout(0.8)		
Dense+Softmax(2)		

for such signals of SGWB in this data is a challenging task, and this topic has been explored by some studies using various methods such as in [35–39].

Particularly, predicted relic gravitational waves (RGWs) originating from the early stages of the Universe, represent one of the most intriguing targets among the SGWB. Detecting the RGWs is of great importance because it provides insights into the evolution of the early Universe and offers crucial evidence for various cosmological models such as the Big Bang theory [40–42]. In this article, we focus on typical models of RGWs from the inflation [30, 43–45] and the first-order phase transition (FOPT) [35, 46–51] that occurred in the early Universe, and we construct effective and targeted deep learning neural networks to search for signals caused by these GWs within the real data of LIGO (O2, O3a and O3b). Such GWs are characterized by distinctive spectral forms, and thus we attempt to identify them according to their characteristic spectra. For the first step, we generate massive simulated samples of these GWs based on corresponding models, and secondly, we establish and train Convolutional Neural Networks (CNNs, see table 1) by using these simulated GW signals mixed with the LIGO data; third, after the training, we verify and confirm that the trained CNN is able to identify these GW signals according to their distinctive properties caused by various parameters. Next, we search for the targeted GW signals by such neural networks among the real LIGO data, to find out the likelihood of the presence of these signals for different orders of magnitude of GW strengths. If no evidence of such signals is found, we can provide corresponding constraints or upper limits.

In addition to traditional methods, research on GWs using CNNs has been fruitful in recent years [52–66]. Some advantages of employing CNN include the following: (i) the convolutional layers in CNN operate by computing over the 'local receptive fields' (local regions) [67] and identifying features in the data through shared weights. Applying the shared weights [56, 67–69] not only reduces the model's complexity but also decreases the number of parameters that need to be learned, thereby improving their computational efficiency, rendering them apt for processing large-scale datasets such as the parameter space discussed in this work. (ii) CNNs combat the problem of the 'curse of dimensionality' (as a common challenge in high-dimensional data analysis) [70, 71], by utilizing their hierarchical structure to reduce dimensionality and aggregate features. CNNs gradually map high-dimensional data into a lower-dimensional feature space through multiple convolutional layers while preserving key patterns. (iii) CNNs can capture intricate non-linear relationships within data and signal features, through their multi-layered structure, making them suitable for analyzing GW signals. The various non-linear activation functions and pooling layers in CNNs further enhance the models' non-linear representation [72, 73]. This capability makes CNNs effective at handling complex pattern recognition tasks. The LIGO data focused here involves parameters and features which exhibit non-linear relations, so in such case they are particularly well-suited for investigation using the deep neural network of CNN.

The theoretical models for the inflation stage we focus on in this article predict RGWs in a wide frequency band of about 10^{-18} to 10^{10} Hz [43–45], and in some parameter range, their amplitude could fall within the sensitivity range of LIGO. The model of FOPT [35] is anticipated to generate components of SGWB through processes involving the bubble nucleation, expansion, collision, and thermalization into light particles [35, 49]. In this model, if the parameter $T_{\rm pt} \sim (10^7 - 10^{10})$ Gev, the resulting SGWB falls within the frequency range of Advanced LIGO and Advanced Virgo [74, 75]. During the FOPT, it has been determined that the GWs can be mainly generated from three sources: bubble collisions, sound waves, and magnetohydrodynamic turbulence [51, 76–78]. Here, we do not consider contribution of the magnetohydrodynamic turbulence, because it always occurs with the sound waves and its strength is secondary; furthermore, we notice that its spectrum is the least known [77, 79–82]. Thus, we mainly consider the GWs generated from the sound waves and bubble collisions during the FOPT.

The plan of this article is as follows: in section 2, we generate simulated GW signals based on typical models, and mix them together with the LIGO data, to prepare the datasets for training and testing for the constructed deep learning neural networks. In section 3, we attempt to identify above GW signals in the LIGO data or estimate the likelihood of the presence of such signals. In section 4, we provide a conclusion and discuss the findings of our research.

2. Generation of samples based on simulated GW signals and the real LIGO data

The SGWB arises from the superposition of a large number of independent GW sources, encompassing various physical phenomena like inflation, phase transitions, and cosmic strings, along with astrophysical processes such as binary mergers; consequently they exhibit a stochastic nature in both temporal and spatial dimensions, with their combined effect demonstrating statistical properties in terms of direction, spectrum, polarization, and other aspects. As one of the most focused targets among SGWB, the RGWs could be generated during the inflationary expansion of the early Universe and have a spectrum distributed over a very wide range of

frequencies. The typical primordial spectrum of such RGWs from inflation (we abbreviate this source as RGWinfl, hereafter) can be expressed as [30]:

$$h(\nu, \tau_i) = A\left(\frac{\nu}{\nu_H}\right)^{2+\beta} A_{\alpha_t}(\nu), \tag{1}$$

where the τ_i is the time of different stages of expansion of the Universe. For the spectra in other frequency ranges, the calculation is the same as [43–45]. In the frequency range of 20-300Hz, it gives [30, 44]:

$$h(\nu, \tau_H) \approx A\left(\frac{\nu}{\nu_H}\right)^{\beta+1} \frac{\nu_H}{\nu_2} \frac{1}{(1+z_E)^{3+\epsilon}} A_{\alpha_t}(\nu). \tag{2}$$

In equation (2), the $A = 4.94 \times 10^{-5} r^{1/2} (\nu_H/\nu_0)^{2+\beta}$; the factor A contains some oscillating factors in the form of $\cos(k\tau_H)$ or $\cos(y_2)$ [44]. The small parameter $\epsilon \equiv (1+\beta)(1-\gamma)/\gamma$, $1 + z_E = (\Omega_\Lambda/\Omega_m)^{1/3}$; Ω_Λ is for dark energy; Ω_m is for dark matter. In this article, we take $\gamma = 1.044$, $\Omega_\Lambda = 0.75$, $\Omega_m = 0.25$, tensor/scalar ratio $r = 0.55$. The τ_H is the present time. The ν_H is the Hubble frequency, $\nu_2/\nu_H = 58.8$, $\nu_0 = 3 \times 10^{-18}$Hz. The inflationary index β is an important model parameter that affects the overall slope of the RGW spectrum. The extra factor [30]

$$A_{\alpha_t}(\nu) \equiv \left(\frac{\nu}{\nu_0}\right)^{(1/4)\alpha_t \ln(\nu/\nu_0)}, \tag{3}$$

is the deviation from a simple power-law spectrum caused by α_t, which reflects the additional curvature. The dimensionless spectral energy density of RGWs can be described as [30]:

$$\Omega_g(\nu) = \frac{\pi^2}{3} h^2(\nu, \tau_H) \left(\frac{\nu}{\nu_H}\right)^2. \tag{4}$$

The energy density spectrum of SGWB is $\Omega_{\rm GW}(f) = {\rm d}\rho_{\rm GW}/(\rho_c {\rm d}\ln f)$; ρ_c is the current critical energy density and $\rho_c = 3c^2 H_0^2/(8\pi G)$. In the most common thermal transitions in the early Universe, the main source of GW production is sound waves in the plasma caused by the coupling between the scalar field and the thermal bath [35, 46–48]. The spectrum from numerical simulations can be expressed as [35]:

$$\Omega_{\rm sw}(f)h^2 = 2.65 \times 10^{-6} \left(\frac{H_{\rm pt}}{\beta}\right) \left(\frac{\kappa_{\rm sw}\alpha}{1+\alpha}\right)^2 \left(\frac{100}{g_*}\right)^{1/3} \times v_w \left(\frac{f}{f_{\rm sw}}\right)^3 \left(\frac{7}{4+3(f/f_{\rm sw})^2}\right)^{7/2} \Upsilon(\tau_{\rm sw}), \tag{5}$$

where $\kappa_{\rm sw}$ is the fraction of vacuum energy converted into bulk fluid kinetic energy; $H_{\rm pt}$ is the Hubble parameter at the temperature $T_{\rm pt}$; g_* is the number of relativistic degrees of freedom, which we take to be 100 in this paper; $f_{\rm sw}$ is the present peak frequency [35]; h is the dimensionless Hubble parameter; v_w is the bubble wall velocity.

$$f_{\rm sw} = 19 \frac{1}{v_w} \left(\frac{\beta}{H_{\rm pt}}\right) \left(\frac{T_{\rm pt}}{100{\rm GeV}}\right) \left(\frac{g_*}{100}\right)^{1/6} \mu{\rm Hz}. \tag{6}$$

$$\Upsilon = 1 - (1 + 2\tau_{\rm sw} H_{\rm pt})^{-1/2}. \tag{7}$$

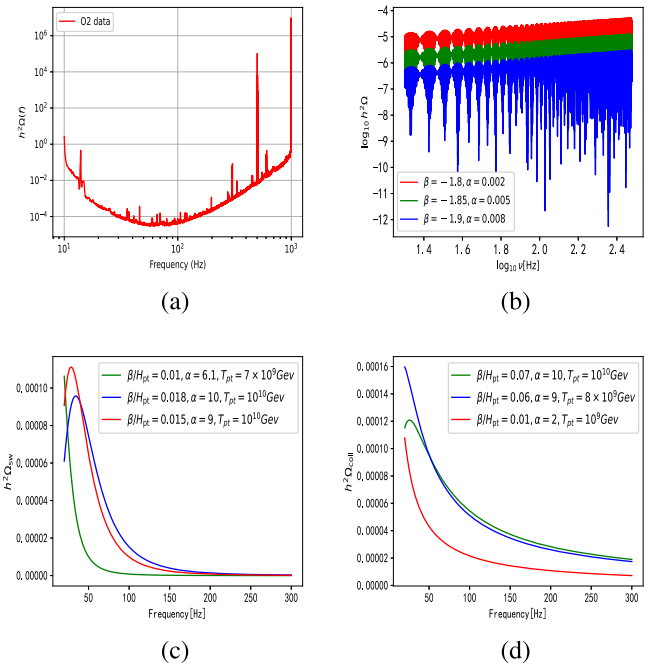

Figure 1. (a) presents the spectral energy density ($h^2\Omega$) of typical O2 data; (b) presents typical spectral energy density ($h^2\Omega$) of RGWinfl; (c) demonstrates the spectral energy density ($h^2\Omega$) of GWs originating from the sound waves for various parameters; (d) demonstrates some example spectral energy density ($h^2\Omega$) of GWs originating from the bubble collisions. The duration for this figure is one second. The vertical axis of (c), (d) is $h^2\Omega$. .

The $\tau_{\rm sw}$ is usually chosen as the time scale of the onset of turbulence [51], $\tau_{\rm sw} \approx R_{\rm pt}/\bar{U}_f$; the scale parameter of exponential nucleation of bubbles $R_{\rm pt} = (8\pi)^{1/3} v_w/\beta$, and $\bar{U}_f^2 = 3\kappa_{\rm sw}\alpha/[4(1+\alpha)]$ [51]. When sound waves and magnetohydrodynamic turbulence are highly suppressed or absent, bubble collisions may dominate, and the GW spectrum can be well modeled by the envelope approximation. The spectrum can be [35, 49, 50]:

$$\Omega_{\rm coll}(f)h^2 = 1.67 \times 10^{-5} \Delta \left(\frac{H_{\rm pt}}{\beta}\right)^2 \left(\frac{\kappa_\phi \alpha}{1+\alpha}\right)^2 \times \left(\frac{100}{g_*}\right)^{1/3} S_{\rm env}(f), \tag{8}$$

where amplitude $\Delta(v_w) = 0.48 v_w^3/(1 + 5.3 v_w^2 + 5 v_w^4)$. The shape of the spectrum is

$$S_{\rm env} = 1/(c_l \tilde{f}^{-3} + (1 - c_l - c_h)\tilde{f}^{-1} + c_h \tilde{f}), \tag{9}$$

where $c_l = 0.064$, $c_h = 0.48$, $\tilde{f} = f/f_{\rm env}$; $f_{\rm env}$ presents the current peak frequency:

$$f_{\rm env} = 16.5 \left(\frac{f_{\rm bc}}{\beta}\right) \left(\frac{\beta}{H_{\rm pt}}\right) \left(\frac{T_{\rm pt}}{100{\rm GeV}}\right) \left(\frac{g_*}{100}\right)^{1/6} \mu{\rm Hz}, \tag{10}$$

$$f_{\rm bc} = 0.35\beta/(1 + 0.069 v_w + 0.69 v_w^4). \tag{11}$$

The characteristic amplitude of GWs can be expressed as [83]:

$$h_{\rm c}(f) \simeq 1.263 \times 10^{-18} (1\ {\rm Hz}/f) \sqrt{h^2 \Omega_{\rm gw}(f)}. \tag{12}$$

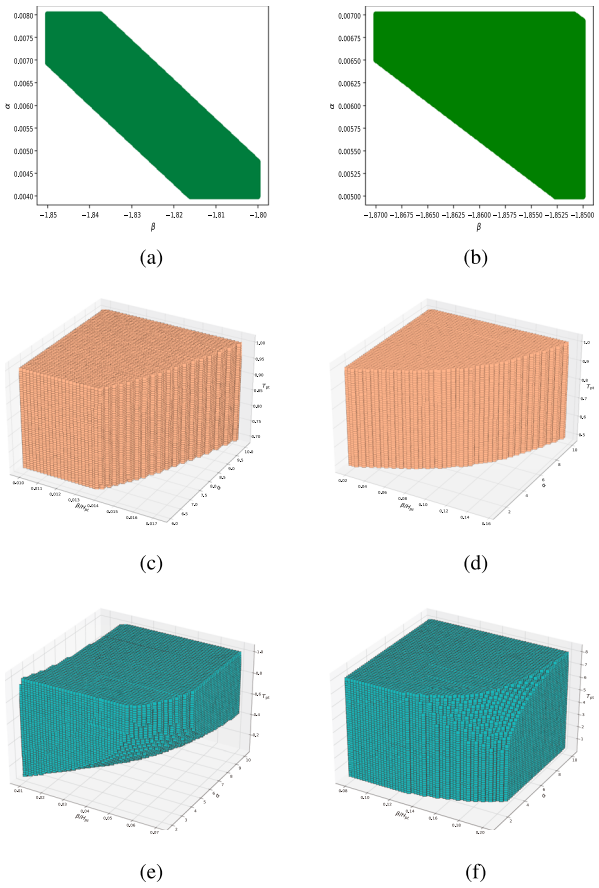

Figure 2. By reverse mapping for parameters of RGW models, (a) and (b) show the parameter boundaries for sets 1 and 2 in table 2, respectively. (c), (d), (e) and (f) display the parameter boundaries for sets 1, 2, 4 and 5 in table 3, respectively.

In our analysis, we take $v_w = 1$, $\kappa_\phi = 1$, and $\kappa_{sw} = \frac{\alpha}{0.73 + 0.083\sqrt{\alpha} + \alpha}$ [35, 51].

We obtain O2 data from Gravitational Wave Open Science Center (GWOSC) [84, 85], e.g., see figure 1(a). The selected segments are from the real strain data, and each dataset contains 1-second time series, with a sampling rate of 4096 Hz. We use PyCBC to filter the datasets, applying a band-pass filter so that only the frequency components within 20-300 Hz remain, and then transform them into the frequency domain. Then we take the modulus of the frequency domain data and divide it by $\sqrt{2}$ to get the characteristic amplitude. The spectral energy density of O2 data can be acquired from equation (12). The O2 data samples we obtained are twice the number of simulated GW signal samples (as described below). We consider three GW models of equations (4), (5) and (8), respectively, e.g., also see figures 1(b)–(d). Although deep neural networks possess generalization capabilities, there is still a possibility of misclassification, especially when there is a large difference in the parameter space. Therefore, in order to ensure the reliability and robustness of the applied method and neural network, we employ reverse mapping (a straightforward process to calculate the parameter boundary according to given certain order of magnitude of GW strength) to acquire the specific boundary (usually not rectangle or cuboid, see figure 2) in parameter space, and thus we generate samples (for deep learning) within these specific parameter regions. For the case of RGWinfl, for each order of magnitude of spectral energy density $h^2\Omega_{\rm GW}$, we take 300 × 300 points sitting in the above mentioned corresponding 2D parameter region within the rectangle of $\beta \times \alpha$ values (see table 2). For GWs from FOPT, for each order of magnitude of spectral energy density $h^2\Omega_{\rm GW}$, we take 50 × 50 × 45 points in the 3D parameter region within the cuboid of $\beta/H_{\rm pt} \times \alpha \times T_{\rm pt}$ (see table 3). Namely, the actual parameter regions we selected are within and smaller than the 'parameter boundary' of table 2 and 3 (also see figure 2); this approach ensures more accurate coverage of the corresponding parameter points and avoids a mismatched parameter selection. In this way, the selected parameter points cover every corresponding order of magnitude of GWs. By generating simulated samples of the above GWs in the forms of spectral energy densities, we overlay them with the spectral energy densities of the O2 data. For all the obtained samples, half are pure O2 data samples and the other half are samples of O2 data plus the simulated GW signals. We split these samples into a training set and test set in a 7:3 ratio.

3. Estimation of likelihood of the presence of the targeted GW signals in real LIGO data by CNN

We construct a suitable one-dimensional CNN model, using the alternation of convolutional layers and pooling layers to extract the features of the samples. The structure of the CNN model is shown in table 1. Before training, we normalize the sample data to a range between 0 and 1, and set up by using ReLU [86] as the activation function, using Categorical Cross-Entropy (CCE) loss function to evaluate the deviation between the predicted values and the actual values, using Adam optimizer [87–89] to optimize the weights and biases of the CNN, and by setting the learning rate to 10^{-5}. Finally, we employ the binary output score s of the network to calculate the confidence that the GW signal is present in the LIGO data through the softmax function [59]:

$$p = \frac{1}{1 + \mathrm{e}^{-s}}. \tag{13}$$

The p-value ranges from 0 to 1 and we adopt it to characterize the confidence that the LIGO data contains these typical RGW signals. In this study, we use 0.5 as the threshold, and the closer the p-value is to 1, the higher the likelihood of the presence of targeted GW signals. In our analysis, we first generate simulated GW signals of different orders of magnitude across various parameter spaces (as mentioned in the section 2), then we train CNNs for signals of each orders of magnitude separately. In each parameter space for the trained CNN model, we calculate the confidence that the real LIGO data (based on the 6000 raw sample obtained by O2, O3a and O3b data, respectively) contains the aforementioned three types of potential RGW signals, and the distributions and mean values are given. Tables 2 and 3, respectively, show the parameter space of the three GW models that we

Table 2. Parameter settings for RGWinfl and the mean value (of p-value) for the confidence of the presence of such GW signals in real LIGO data (O2, O3a and O3b). The 'Recognition accuracy' is for the constructed CNN in determining whether the test data is mixed with the simulated GW signals.

Set	Parameter boundary	Magnitude of $h^2\Omega_{\rm GW}$	$\sqrt{PSD}$ ($Hz^{-1/2}$)	Recognition accuracy	Mean p-value for O2 data plus simulated GW signals	Mean p-value (O2)	Mean p-value (O3a)	Mean p-value (O3b)
1	$\beta \in (-1.85, -1.8)$ $\alpha \in (0.004, 0.008)$	$\sim 10^{-4}$	$\sim 10^{-22}$	0.9982	0.99986713	0.00776	3.15×10^{-7}	3.37×10^{-5}
2	$\beta \in (-1.87, -1.85)$ $\alpha \in (0.005,\ 0.007)$	$\sim 10^{-5}$	$\sim 10^{-23}$	0.9422	0.9033364	0.10817	0.0035649	0.0005467
3	$\beta \in (-1.91, -1.88)$ $\alpha \in (0.006,\ 0.008)$	$\sim 10^{-6}$	$\sim 10^{-24}$	0.4961 (Unrecognized)	0.501124	0.498391	0.4884417	0.487882
4	$\beta \in (-2.0, -1.92)$ $\alpha \in (0.007,\ 0.008)$	$\sim 10^{-7}$ to $\sim 10^{-10}$	$\sim 10^{-25}$ to $\sim 10^{-28}$	0.4917 (Unrecognized)	0.5022312	0.500165	0.498763	0.489765

Table 3. Parameter settings for the GWs from FOPT and the mean p-value for the confidence of the presence of these GW signals in real LIGO data (O2, O3a and O3b).

Set	Parameter boundary	Magnitude of $h^2\Omega_{GW}$	$\sqrt{PSD}$ $(Hz^{-1/2})$	Recognition accuracy	Mean p-value for O2 data plus simulated GW signals	Mean p-value (O2)	Mean p-value (O3a)	Mean p-value (O3b)
GWs originating from sound waves								
1	$\beta/H_{pt} \in (0.01, 0.019)$ $\alpha \in (6.1, 10)$ $T_{pt} \in (7 \times 10^9, 10^{10})$Gev	$\sim 10^{-4}$	$\sim 10^{-22}$	0.9994	0.994755	0.02574	4×10^{-6}	1×10^{-4}
2	$\beta/H_{pt} \in (0.02, 0.16)$ $\alpha \in (1, 10)$ $T_{pt} \in (5 \times 10^9, 10^{10})$Gev	$\sim 10^{-5}$	$\sim 10^{-23}$	0.9494	0.94873	0.12302	0.00151	0.00058
3	$\beta/H_{pt} \in (0.17, 0.4)$ $\alpha \in (1.1, 10)$ $T_{pt} \in (5 \times 10^8, 10^{10})$Gev	$\sim 10^{-6}$	$\sim 10^{-24}$	0.5012 (Unrecognized)	0.499987	0.49341	0.48976	0.48875
GWs originating from bubble collisions								
4	$\beta/H_{pt} \in (0.01, 0.07)$ $\alpha \in (2, 10)$ $T_{pt} \in (10^9, 10^{10})$Gev	$\sim 10^{-4}$	$\sim 10^{-22}$	0.9998	0.999396	0.002406	6×10^{-5}	1×10^{-5}
5	$\beta/H_{pt} \in (0.08, 0.2)$ $\alpha \in (1, 10)$ $T_{pt} \in (5 \times 10^9, 8 \times 10^{10})$Gev	$\sim 10^{-5}$	$\sim 10^{-23}$	0.9683	0.968897	0.062567	0.002691	0.001658
6	$\beta/H_{pt} \in (0.3, 0.7)$ $\alpha \in (4, 10)$ $T_{pt} \in (2 \times 10^8, 10^{10})$Gev	$\sim 10^{-6}$	$\sim 10^{-24}$	0.4992 (Unrecognized)	0.50231	0.49654	0.49002	0.48532

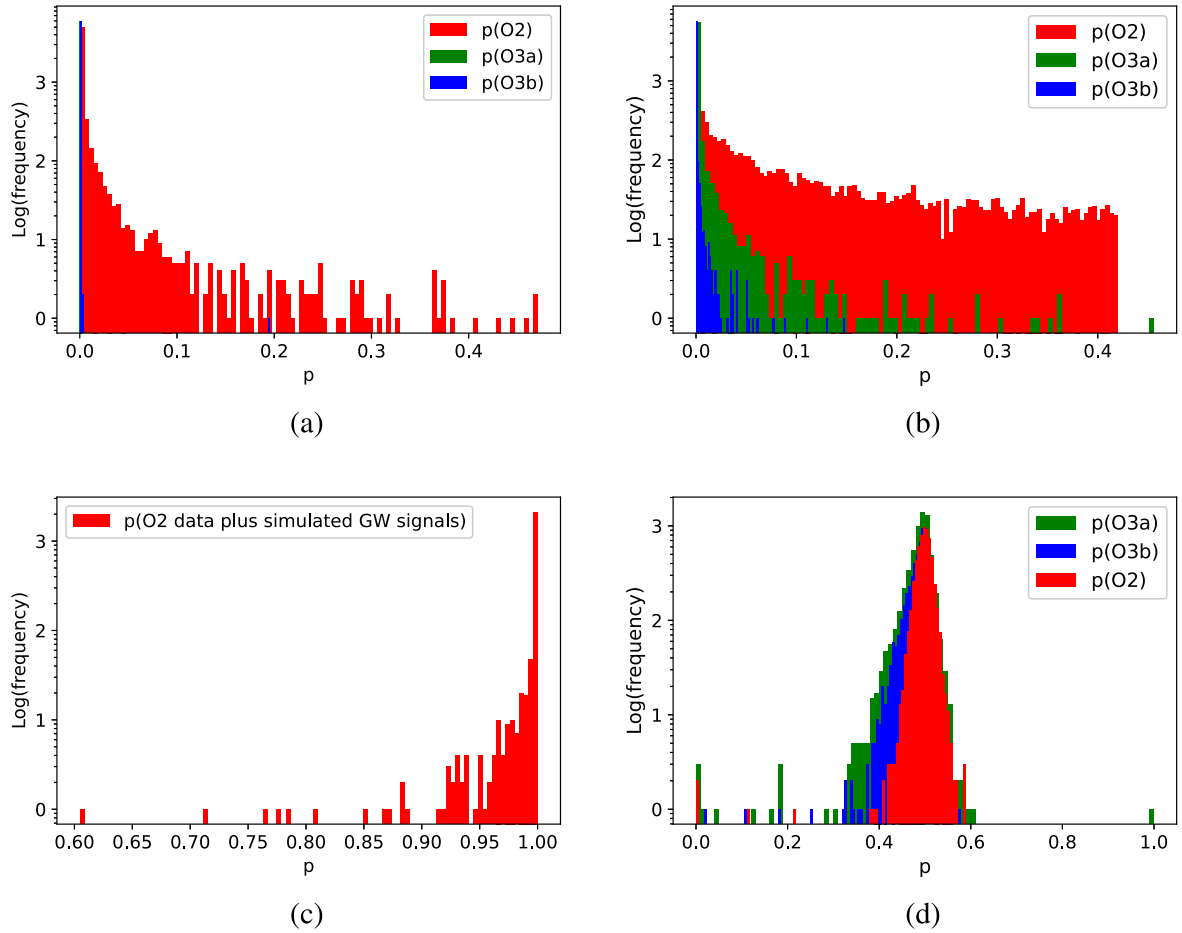

Figure 3. (a), (b) and (d) show the distribution of the confidence of containing typical targeted RGWs in the O2, O3a and O3b data for sets 1, 2 and 3 in table 2, respectively. The red, green and blue lines represent the distribution of the confidence of containing RGWs in the 6000 samples from the O2, O3a and O3b data, respectively. (c) illustrates the distribution of the confidence of containing simulated RGWs in the O2 data for set 1 in table 2. The x-axis represents the distribution of p-values; the y-axis represents the Log distribution frequency, i.e., we divided the distribution of p-value of 6000 samples into 100 narrow intervals, and count the number of samples with p-value sitting in each interval.

consider, and corresponding mean values of the confidence or likelihood.

For the adjustment and adaptation processes, we initiated the construction of a CNN model with multiple convolutional layers and pooling layers, evaluating potential overfitting or underfitting by monitoring accuracy during training and testing as the epochs progressed. In cases of overfitting, we simplified the network structure by removing certain convolutional and pooling layers, whereas underfitting prompted the addition of layers to enhance the network's complexity. Typically, we set the learning rate in the range of 10^{-3} to 10^{-5}, recognizing that excessively high learning rates could compromise optimal training results. To address the overfitting, we also implemented the dropout technique to deactivate specific neurons, making the network more concise with enhanced efficiency. Through these adjustments, we successfully developed neural networks that have overcome the overfitting and underfitting challenges, enabling the CNNs to perform effectively on both training and test sets, achieving an optimal state.

From set 1 and 2 in table 2 and figures 3(a) and (b), we can see that when the parameter spaces of RGWinfl are $[\beta \in (-1.85, -1.8), \alpha \in (0.004, 0.008)]$ and $[\beta \in (-1.87, -1.85), \alpha \in (0.005, 0.007)]$, the magnitude of spectral energy density of RGWinfl is $\sim 10^{-4}$ and $\sim 10^{-5}$; the recognition accuracy (the accuracy of the built CNN in determining whether the test data is mixed with the simulated GW signals, in addition to the real LIGO data) of the constructed CNN is around 0.99; the distributions of the confidence of containing RGWs in the 6000 samples from the O2, O3a and O3b data are less than 0.5, or, we found no evidence of presence of these RGWs. From set 3 in table 2 and figure 3(d), we can see that when the parameter space of the RGWs is $[\beta \in (-1.91, -1.88), \alpha \in (0.006, 0.008)]$, the magnitude of the spectral energy density of RGWs is $\sim 10^{-6}$; the recognition accuracy of the built CNN is around 0.49; some of the 6000 sample data in O2, O3a and O3b seem to contain RGW signals with confidence greater than 0.5, but we find that this is just due to the false positives (the reason is due to the invalidation of recognition for the GW signal parameters, this will be explained later).

From set 1 and 2 in table 3 and figures 4(a) and (b), we can see that for GWs from FOPT (sound wave case), where the parameter spaces of the GWs are $[\beta/H_{\rm pt} \in (0.01, 0.019),$

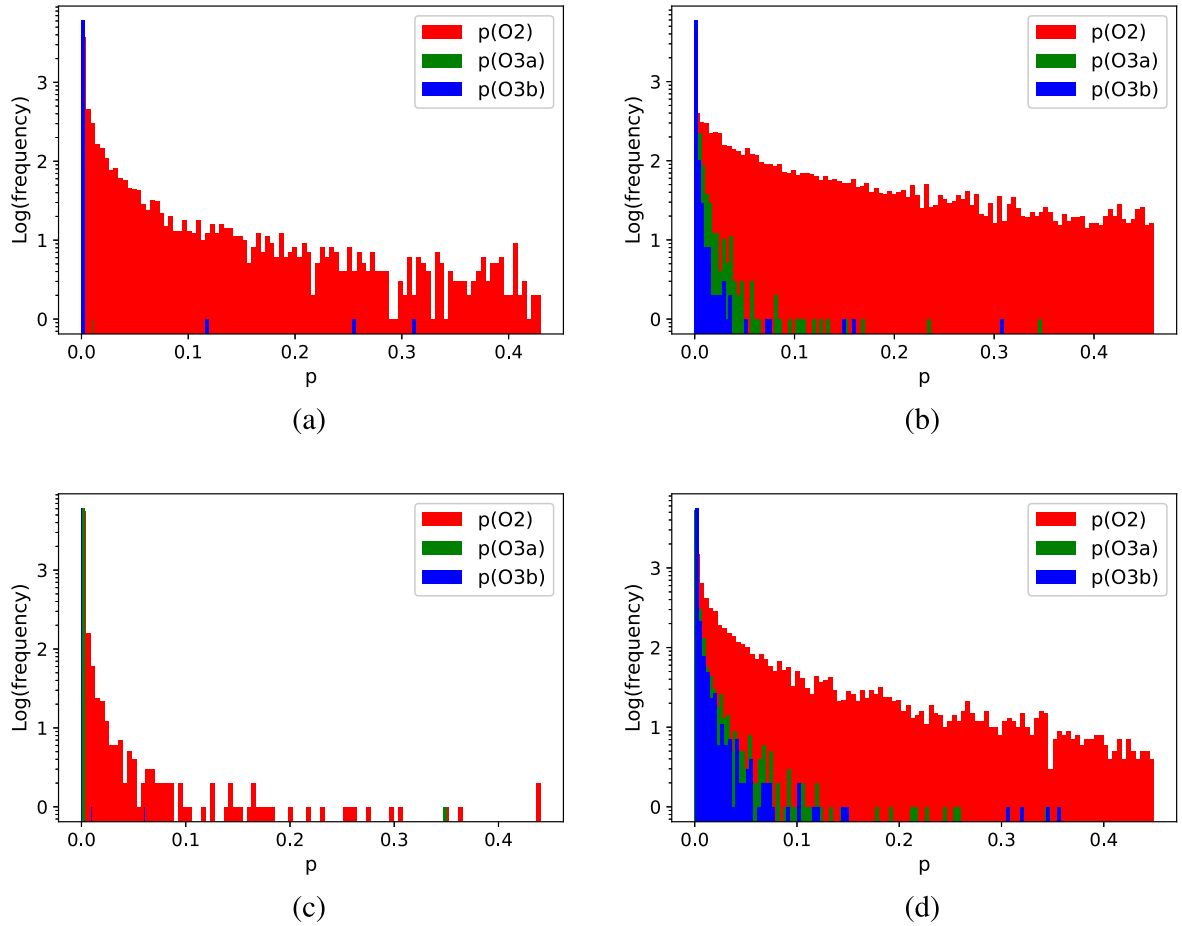

Figure 4. (a), (b), (c) and (d) demonstrate the distributions of the confidence of containing the GWs from FOPT in the O2, O3a and O3b data for sets 1, 2, 4 and 5 in table 3, respectively. The red, green and blue lines represent the distribution of the confidence of containing the GWs from FOPT in the 6000 samples from the O2, O3a and O3b data, respectively. The y-axis represents the Log distribution frequency.

$\alpha \in (6.1,\ 10)$, $T_{\rm pt} \in (7 \times 10^9,\ 10^{10})$ Gev] and [$\beta/H_{\rm pt} \in (0.02,\ 0.16)$, $\alpha \in (1,\ 10)$, $T_{\rm pt} \in (5 \times 10^9,\ 10^{10})$ Gev], the magnitude of the spectral energy density of GWs is $\sim 10^{-4}$ and $\sim 10^{-5}$; the recognition accuracy of the built CNN is around 0.99; the distributions of confidence of the containing GWs in the 6000 samples from the O2, O3a and O3b data are less than 0.5, or , we found no evidence of the presence of such GW signals in the O2, O3a or O3b data. From set 4 and 5 in table 3 and figures 4(c) and (d), when GWs originated from the bubble collisions, where the parameter spaces of GWs are [$\beta/H_{\rm pt} \in (0.01,\ 0.07)$, $\alpha \in (2,\ 10)$, $T_{\rm pt} \in (10^9,\ 10^{10})$ Gev] and [$\beta/H_{\rm pt} \in (0.08,\ 0.2)$, $\alpha \in (1,\ 10)$, $T_{\rm pt} \in (5 \times 10^9,\ 8 \times 10^{10})$ Gev], the magnitude of spectral energy density of GWs is $\sim 10^{-4}$ and $\sim 10^{-5}$; the recognition accuracy of established CNN is close to 0.99; the confidences is less than 0.5, thereby finding no evidence of the presence of such GW signals in the data from O2, O3a or O3b.

Next, we use constructed CNN (table 1) to estimate the parameters of GW signals. The purpose of this task is to check whether the networks we establish really have sufficiently acquired the ability to recognize the features and parameters of the signals. We consider three GW models of equations (4), (5) and (8), respectively. For each type of GW model, within the parameter spaces, we obtained a total of 100,000 O2 data samples containing simulated GW signals. We use the mean squared error (MSE) loss function to evaluate the deviation between the predicted and true values. In the final layer, we use the linear activation function to output the predicted values. From figures 5(a) (b) and 6, it is evident that our network model can recognize the characteristics of GW signals by correctly estimating their corresponding multiple parameters. As mentioned earlier, the selected sample points can cover the parameter regions corresponding to each order of magnitude of the GW signals. Moreover, for dividing the training and testing sets, we also follow the principle of random distribution. Therefore, our network can reliably and robustly identify these GW signals in specific orders of magnitude within the parameter regions. This ability is based on the confirmed capability of the network to recognize these concrete parameters, rather than relying on other arbitrary criteria or simply distinguishing between the presence or absence of any unknown signals. For example, as shown in table 3 (line 5), the model exhibits a very high recognition accuracy, so if any GW signal within the corresponding parameter region appears, we have reason to believe in its presence. If the test on the real LIGO data yields a null result, such an output is also reliable, at least for the region of parameters we are concerned with. In contrast,

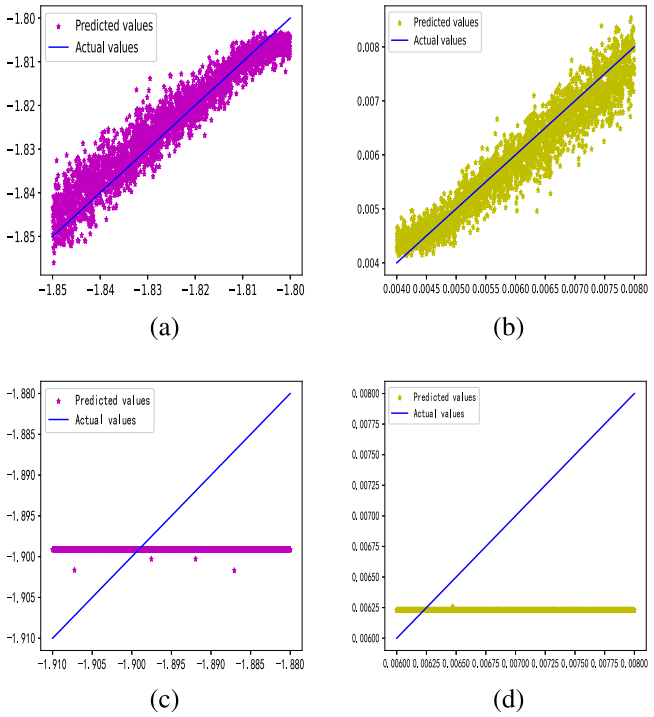

Figure 5. (a) and (b) express the results of simultaneous estimation of GW parameters β and α for 10000 samples in set 1 of table 2. Here $\beta \in (-1.85, -1.8)$, $\alpha \in (0.004, 0.008)$. The residuals are 0.00071 and 0.00025, respectively. (c) and (d) display the results of simultaneous estimation of β and α for 10000 samples in set 3 of table 2. Here $\beta \in (-1.91, -1.88)$, $\alpha \in (0.006, 0.008)$. Importantly, the results shown in (c) and (d) indicate that for such order of magnitude of GW signals, the built CNN cannot correctly recognize or estimate corresponding GW parameters, so in such case the p-value given by the CNN is not reliable, and this is also the reason for the false positive in (d) of figure 3.

the results shown in figures 5(c) and (d) indicate that for the order of magnitude ($\sim 10^{-6}$) of RGWinfl signals, the built CNN has no ability to correctly recognize the characteristics of the RGWinfl signals, or, their parameters cannot be properly estimated, and this is also the reason for the false positive in figure 3(d). Here, please also notice that, the parameter ranges in figure 5 are small, and such ranges are also calculated by the reverse mapping process mentioned above. For instance, in figure 2(a) we can find the range of α from 0.004 to 0.008, the same as in figure 5(b), corresponding to $h^2\Omega_{\rm GW} \sim 10^{-4}$, which can also be found consistently in table 2 (set 1). It is the same for parameter β in figure 5.

In traditional methods used to constrain GWs, some noises are uncorrelated between different detectors, so utilizing the cross-correlation relationship between two detectors helps achieve higher sensitivity usually by several orders of magnitude, and such correlation can be quantified by the overlap reduction function [90, 91] (a dimensionless function of frequency encoding relative locations and orientations of GW detector pair), and these topics have been extensively investigated in previous studies like [90–107]. Particularly, focusing on the SGWB, the LIGO Scientific Collaboration, Virgo Collaboration and KAGRA Collaboration, reported a series of results by use of cross-correlation (overlap reduction function) for the O1, O2 and O3 runs. For example, in 2017, the [98] for O1 provided $\Omega_0 < 1.7 \times 10^{-7}$, and comparatively, our result in this article, the $h^2\Omega_{\rm GW}$ is in the level of 10^{-5} (see tables 2 and 3; the 'h' is the reduced Hubble parameter with a value of about 0.6). Later, in the 2018 paper [99] and 2019 paper [102] for O1 and O2, the reported sensitivities gradually increased, and in the 2021 paper [104] for O3, the upper limit of $\Omega_{\rm GW}$ was suppressed into 10^{-9}. These results (giving lower upper limits) are more accurate than what we obtain by the CNN here, and this is mainly due to the limitations of the current structure of the neural network that we use, e.g., not benefited by the cross-correlation relationship. However, through our study as an exploration, we have recognized how to ensure the reliability of the results produced by the aforementioned deep learning neural networks, e.g., as shown in figure 5, when the GW parameters can be correctly recognized and estimated for specific GW strengths, the obtained high p-value and corresponding upper limit are reliable and adoptable. Thus, holding such premises and guidelines, we will endeavor to develop more advanced CNN architectures or more complex neural networks, such as those leveraging the cross-correlation, to achieve enhanced sensitivity and improved upper limits in the future. These anticipated efforts involve massive computation and fundamental modifications, and we shall try to pursue such studies in subsequent works.

4. Conclusion and discussion

In this work, we search for typical RGWs (from the early stages of the Universe as key components of SGWB) in the real LIGO data. Our focus is primarily on RGWs from the inflation and the FOPT (by sound waves and bubble collisions). By adjustment and adaptation processes, we successfully establish effective and targeted deep learning neural networks to calculate the likelihood of the presence of the above RGWs in the real LIGO data. Additionally, we attempt to estimate their relevant parameters and provide constraints on strengths of these RGWs. We find the following results:

1. When the parameter region of RGWinfl are within $[\beta \in (-1.85, -1.8), \alpha \in (0.004, 0.008)]$ and $[\beta \in (-1.87, -1.85), \alpha \in (0.005, 0.007)]$ (the corresponding magnitudes of the spectral energy density of RGWinfl are $\sim 10^{-4}$ and $\sim 10^{-5}$), the distributions of the confidence of containing RGWinfl in the 6000 samples from the real LIGO data O2, O3a and O3b is less than 0.5, or, we found no evidence of the presence of RGWinfl signals in these data. When the parameter region of RGWinfl are within $[\beta \in (-1.91, -1.88), \alpha \in (0.006, 0.008)]$ (the corresponding magnitude of spectral energy density of RGWinfl is $\sim 10^{-6}$), some of the 6000 sample data in O2, O3a and O3b seem to contain RGW signals with confidence greater than 0.5; however, this result is due to the false positive, explained in section 3, (also see figure 5), that, when the constructed CNN cannot correctly estimate the parameters of the predicted GWs, the given p-value is not reliable or adoptable.

2. For the GWs from FOPT (sound wave case), with the parameter region within $[\beta/H_{\rm pt} \in (0.01, 0.019), \alpha \in (6.1, 10), T_{\rm pt} \in (7 \times 10^9, 10^{10})$ Gev] and $[\beta/H_{\rm pt} \in (0.02, 0.16),$

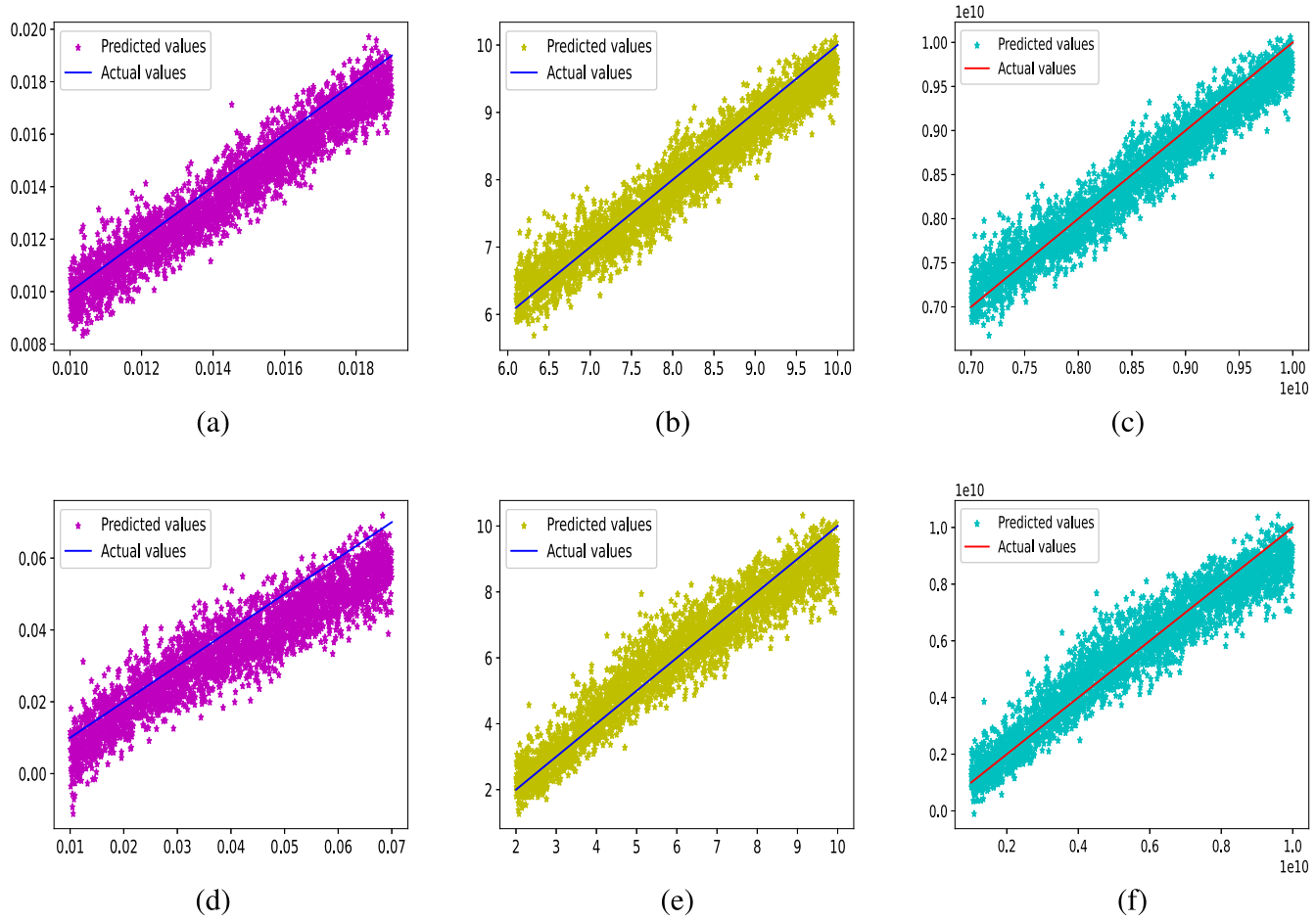

Figure 6. (a), (b) and (c) demonstrate the results of simultaneous estimation of parameters $\beta/H_{\rm pt}$, α and $T_{\rm pt}$ for 10000 samples in set 1 of table 3. Here $\beta/H_{\rm pt} \in (0.01, 0.019)$, $\alpha \in (6.1, 10)$, $T_{\rm pt} \in (7 \times 10^9, 10^{10})$Gev. The residuals are 0.000148, 0.0354 and 0.01026, respectively. (c), (d) and (e) show the results of simultaneous estimation of parameters $\beta/H_{\rm pt}$, α and $T_{\rm pt}$ for 10000 samples in set 4 of table 3. Here $\beta/H_{\rm pt} \in (0.01, 0.07)$, $\alpha \in (2, 10)$, $T_{\rm pt} \in (10^9, 10^{10})$Gev. The residuals are 0.00498, 0.01611 and 0.00148, respectively. The solid lines represent the actual values, and the dots represent the predicted values; these parameters are correctly estimated for the above cases.

$\alpha \in (1, 10)$, $T_{\rm pt} \in (5 \times 10^9, 10^{10})$ Gev] (the corresponding magnitudes of spectral energy density of GWs are $\sim 10^{-4}$ and $\sim 10^{-5}$), the distributions of the confidence of containing GWs in the 6000 samples from the real LIGO data O2, O3a and O3b are less than 0.5, or, we found no evidence of the presence of such GW signals in this data. For the case of GWs from the bubble collisions, for the parameter region within [$\beta/H_{\rm pt} \in (0.01, 0.07)$, $\alpha \in (2, 10)$, $T_{\rm pt} \in (10^9, 10^{10})$ Gev] and [$\beta/H_{\rm pt} \in (0.08, 0.2)$, $\alpha \in (1, 10)$, $T_{\rm pt} \in (5 \times 10^9, 8 \times 10^{10})$ Gev] (the corresponding magnitudes of spectral energy density of the GWs are $\sim 10^{-4}$ and $\sim 10^{-5}$), the distributions of the confidence of containing such GWs in the 6000 samples from the real LIGO data O2, O3a and O3b are also less than 0.5, or, the same, we found no evidence of their presence.

In fact, deep neural networks may result in misclassifications by failing to capture certain features of the signals, due to their limited generalization ability. However, in this paper, the selected sample points cover the corresponding parameter regions for different orders of magnitude, thereby minimizing potential omissions. Furthermore, the neural network's binary classification decisions may also be affected by the presence of other false signals. However, through parameter estimation, we observe that the model possesses excellent capabilities for parameter recognition. In other words, these abilities rely on accurate estimations of specific parameters, thereby avoiding other false signals to be identified as true signals (as also described in the final part of section 3). For instance, when the GW parameters can be correctly recognized and estimated for cases with a specific order of magnitude of GW strengths [figure 5(a), (b) and figure 6], if the simulated GW signals are included in the test data, the established CNN consistently gives very high 'recognition accuracy' and very high p-value [see sets 1 and 2 of table 2, and sets 1, 2, 4 and 5 of table 3, and figure 3(c)]. Thus, if the given p-value is low, it is believable that there is no presence of the targeted GWs. Conversely, when the GW parameters cannot be correctly estimated for cases with certain GW strengths [e.g. Figure 5(c) and (d)], even if the test data does contain the simulated GW signals, the CNN gives low recognition accuracy and low p-value (e.g. set 3 of table 2). For this situation, even if the CNN gives p-values greater than the threshold of 0.5 after testing some data [e.g. Figure 3(d)], this still does not serve as adoptable evidence for the presence of such GW signals (treated as false positive).

Therefore, based on the above considerations and operations, we suggest that the acquired results in this work are reliable.

Briefly, the results indicate no evidence of the presence of the targeted GWs from 1) inflation, 2) sound waves, or 3) bubble collisions, predicted by typical models. For these three cases, the results provide upper limits of their GW spectral energy densities, respectively as: 1) $h^2\Omega_{\rm GW} \sim 10^{-5}$ [correspondingly in a 2D parameter region within boundary of $\beta \in (-1.87, -1.85) \times \alpha \in (0.005, 0.007)$], and 2) $h^2\Omega_{\rm GW} \sim 10^{-5}$ [in a 3D parameter region within a boundary of $\beta/H_{\rm pt} \in (0.02, 0.16) \times \alpha \in (1, 10) \times T_{\rm pt} \in (5 \times 10^9, 10^{10})$ Gev], and 3) $h^2\Omega_{\rm GW} \sim 10^{-5}$ [in a 3D parameter region within a boundary of $\beta/H_{\rm pt} \in (0.08, 0.2) \times \alpha \in (1, 10) \times T_{\rm pt} \in (5 \times 10^9, 8 \times 10^{10})$ Gev]. Although only null results and upper limits are obtained here, our analysis suggests that the above methods and neural networks are effective and reliable, which can be applied not only for the current data but also for the upcoming O4 data. Furthermore, we will endeavor to develop more advanced CNN architectures or more complex neural networks, such as those leveraging cross-correlation, to achieve enhanced sensitivity and refined upper limits in the future, to explore possible RGWs from the early stages of the Universe or provide constraints on relevant cosmological theories. These efforts will be pursued in subsequent works.

Acknowledgments

This work was supported in part by the National Natural Science Foundation of China under Grant Nos. 11605015, 12347101 and 12147102, the Natural Science Foundation Project of Chongqing under Grant No. cstc2020jcyj-msxmX0944, and the Research Funds for the Central Universities under Grant No. 2022CDJXY-002).

ORCID iDs

Hao Wen https://orcid.org/0000-0003-4087-6456

References

[1] The LIGO Scientific Collaboration the Virgo Collaboration the KAGRA Collaboration 2023 arXiv:2111.03606
[2] The LIGO Scientific Collaboration 2021 https://www.ligo.org/
[3] The Virgo Collaboration 2021 https://www.virgo-gw.eu/
[4] Akutsu T *et al* 2021 arXiv:2009.09305
[5] Maggiore M 2000 Gravitational wave experiments and early universe cosmology *Phys. Rep.* **331** 283
[6] Regimbau T 2011 The astrophysical gravitational wave stochastic background *Res. Astron. Astrophys.* **11** 369
[7] Rosado P A 2011 Gravitational wave background from binary systems *Phys. Rev.* D **84** 084004
[8] Wu C, Mandic V and Regimbau T 2012 Accessibility of the gravitational-wave background due to binary coalescences to second and third generation gravitational-wave detectors *Phys. Rev.* D **85** 104024
[9] Zhu X-J, Howell E J, Blair D G and Zhu Z-H 2013 On the gravitational wave background from compact binary coalescences in the band of ground-based interferometers *Mon. Not. R. Astron. Soc.* **431** 882
[10] Lasky P D, Bennett M F and Melatos A 2013 Stochastic gravitational wave background from hydrodynamic turbulence in differentially rotating neutron stars *Phys. Rev.* D **87** 063004
[11] Rosado P A 2012 Gravitational wave background from rotating neutron stars *Phys. Rev.* D **86** 104007
[12] Ferrari V, Matarrese S and Schneider R 1999 Stochastic background of gravitational waves generated by a cosmological population of young, rapidly rotating neutron stars *Mon. Not. R. Astron. Soc.* **303** 258
[13] Buonanno A, Sigl G, Raffelt G G, Janka H-T and Müller E 2005 Stochastic gravitational-wave background from cosmological supernovae *Phys. Rev.* D **72** 084001
[14] Howell E, Coward D, Burman R, Blair D and Gilmore J 2004 The gravitational wave background from neutron star birth throughout the cosmos *Mon. Not. R. Astron. Soc.* **351** 1237
[15] Sandick P, Olive K A, Daigne F and Vangioni E 2006 Gravitational waves from the first stars *Phys. Rev.* D **73** 104024
[16] Zhu X-J, Howell E and Blair D 2010 Observational upper limits on the gravitational wave production of core collapse supernovae *Mon. Not. R. Astron. Soc. Lett.* **409** L132
[17] Crocker K, Mandic V, Regimbau T, Belczynski K, Gladysz W, Olive K, Prestegard T and Vangioni E 2015 Model of the stochastic gravitational-wave background due to core collapse to black holes *Phys. Rev.* D **92** 063005
[18] Crocker K, Prestegard T, Mandic V, Regimbau T, Olive K and Vangioni E 2017 Systematic study of the stochastic gravitational-wave background due to stellar core collapse *Phys. Rev.* D **95** 063015
[19] Kibble T W B 1976 Topology of cosmic domains and strings *J. Phys. A: Math. Gen.* **9** 1387
[20] Sarangi S and Tye S-H 2002 Cosmic string production towards the end of brane inflation *Phys. Lett.* B **536** 185
[21] Damour T and Vilenkin A 2005 Gravitational radiation from cosmic (super)strings: Bursts, stochastic background, and observational windows *Phys. Rev.* D **71** 063510
[22] Siemens X, Mandic V and Creighton J 2007 Gravitational-wave stochastic background from cosmic strings *Phys. Rev. Lett.* **98** 111101
[23] Damour T and Vilenkin A 2000 Gravitational wave bursts from cosmic strings *Phys. Rev. Lett.* **85** 3761
[24] Caldwell R R and Allen B 1992 Cosmological constraints on cosmic-string gravitational radiation *Phys. Rev.* D **45** 3447
[25] Ölmez S, Mandic V and Siemens X 2010 Gravitational-wave stochastic background from kinks and cusps on cosmic strings *Phys. Rev.* D **81** 104028
[26] Witten E 1984 Cosmic separation of phases *Phys. Rev.* D **30** 272
[27] Kosowsky A, Turner M S and Watkins R 1992 Gravitational waves from first-order cosmological phase transitions *Phys. Rev. Lett.* **69** 2026
[28] Dev P S B and Mazumdar A 2016a Probing the scale of new physics by Advanced LIGO/VIRGO *Phys. Rev.* D **93** 104001
[29] Starobinsky A A 1979 Spectrum of relict gravitational radiation and the early state of the universe *JETP Lett.* **30** 682
[30] Tong M L and Zhang Y 2009 Relic gravitational waves with a running spectral index and its constraints at high frequencies *Phys. Rev.* D **80** 084022
[31] Bar-Kana R 1994 Limits on direct detection of gravitational waves *Phys. Rev.* D **50** 1157
[32] Turner M S 1997 Detectability of inflation-produced gravitational waves *Phys. Rev.* D **55** R435

[33] Mandic V, Bird S and Cholis I 2016 Stochastic gravitational-wave background due to primordial binary black hole mergers *Phys. Rev. Lett.* **117** 201102
[34] Martin X and Vilenkin A 1996 Gravitational wave background from hybrid topological defects *Phys. Rev. Lett.* **77** 2879
[35] Romero A, Martinovic K, Callister T A, Guo H-K, Martìnez M, Sakellariadou M, Yang F-W and Zhao Y 2021 Implications for first-order cosmological phase transitions from the third LIGO-Virgo observing run *Phys. Rev. Lett.* **126** 151301
[36] Jiang Y and Huang Q-G 2023 Upper limits on the polarized isotropic stochastic gravitational-wave background from advanced LIGO-Virgo's first three observing runs *J. Cosmol. Astropart. Phys.* **2023** 026
[37] Tsukada L, Callister T, Matas A and Meyers P 2019 First search for a stochastic gravitational-wave background from ultralight bosons *Phys. Rev.* D **99** 103015
[38] Yang K Z, Suresh J, Cusin G, Banagiri S, Feist N, Mandic V, Scarlata C and Michaloliakos I 2023 Measurement of the cross-correlation angular power spectrum between the stochastic gravitational wave background and galaxy overdensity *Phys. Rev.* D **108** 043025
[39] De Lillo F, Suresh J and Miller A L 2022 Stochastic gravitational-wave background searches and constraints on neutron-star ellipticity *Mon. Not. R. Astron. Soc.* **513** 1105
[40] Thorne K S 1987 *Gravitational Radiation: In 300 Years of Gravitation* ed S W Hawking and W Israel (Cambridge: Cambridge University Press)
[41] Thorne K 1995 Particle and nuclear astrophysics and cosmology in the next millenium *Proceedings of the 1994 Snowmass Summer Study held* **29** 160
[42] Schutz B F 1999 Gravitational wave astronomy *Class. Quantum Grav.* **16** A131
[43] Zhang Y, Yuan Y, Zhao W and Chen Y-T 2005 Relic gravitational waves in the accelerating Universe *Class. Quantum Grav.* **22** 1383
[44] Zhang Y, Er X Z, Xia T Y, Zhao W and Miao H X 2006 An exact analytic spectrum of relic gravitational waves in an accelerating universe *Class. Quantum Grav.* **23** 3783
[45] Miao H X and Zhang Y 2007 Analytic spectrum of relic gravitational waves modified by neutrino free streaming and dark energy *Phys. Rev.* D **75** 104009
[46] Hindmarsh M, Huber S J, Rummukainen K and Weir D J 2015 Numerical simulations of acoustically generated gravitational waves at a first order phase transition *Phys. Rev.* D **92** 123009
[47] Hindmarsh M, Huber S J, Rummukainen K and Weir D J 2014 Gravitational waves from the sound of a first order phase transition *Phys. Rev. Lett.* **112** 041301
[48] Hindmarsh M, Huber S J, Rummukainen K and Weir D J 2017 Shape of the acoustic gravitational wave power spectrum from a first order phase transition *Phys. Rev.* D **96** 103520
[49] Jinno R and Takimoto M 2017 Gravitational waves from bubble collisions: an analytic derivation *Phys. Rev.* D **95** 024009
[50] Huber S J and Konstandin T 2008 Gravitational wave production by collisions: more bubbles *J. Cosmol. Astropart. Phys.* **2008** 022
[51] Weir D J 2018 Gravitational waves from a first-order electroweak phase transition: a brief review *Philos. Trans. Royal Soc. A: Math. Phys. Eng. Sci.* **376** 20170126
[52] George D and Huerta E 2018a Deep Learning for real-time gravitational wave detection and parameter estimation: Results with Advanced LIGO data *Phys. Lett.* B **778** 64
[53] George D, Shen H and Huerta E A 2018 Classification and unsupervised clustering of LIGO data with deep transfer learning *Phys. Rev.* D **97** 101501
[54] George D and Huerta E A 2018b Deep neural networks to enable real-time multimessenger astrophysics *Phys. Rev.* D **97** 044039
[55] Razzano M and Cuoco E 2018 Image-based deep learning for classification of noise transients in gravitational wave detectors *Class. Quantum Grav.* **35** 095016
[56] George D and Huerta E A 2018c Deep neural networks to enable real-time multimessenger astrophysics *Phys. Rev.* D **97** 044039
[57] Gabbard H, Williams M, Hayes F and Messenger C 2018 Matching matched filtering with deep networks for gravitational-wave astronomy *Phys. Rev. Lett.* **120** 141103
[58] Dreissigacker C, Sharma R, Messenger C, Zhao R and Prix R 2019 Deep-learning continuous gravitational waves *Phys. Rev.* D **100** 044009
[59] Wang H, Wu S, Cao Z, Liu X and Zhu J-Y 2020 Gravitational-wave signal recognition of LIGO data by deep learning *Phys. Rev.* D **101** 104003
[60] Li X-R, Yu W-L, Fan X-L and Babu G J 2020 Some optimizations on detecting gravitational wave using convolutional neural network *Front. Phys.* **15** 54501
[61] Krastev P G 2020 Real-time detection of gravitational waves from binary neutron stars using artificial neural networks *Phys. Lett.* B **803** 135330
[62] Cuoco E *et al* 2020 Enhancing gravitational-wave science with machine learning *Mach. Learn.: Sci. Technol.* **2** 011002
[63] Wei W and Huerta E 2020 Gravitational wave denoising of binary black hole mergers with deep learning *Phys. Lett.* B **800** 135081
[64] Lin B-J, Li X-R and Yu W-L 2019 Binary neutron stars gravitational wave detection based on wavelet packet analysis and convolutional *Front. Phys.* **15** 24602
[65] Luo H-M, Lin W, Chen Z-C and Huang Q-G 2019a Extraction of gravitational wave signals with optimized convolutional neural network *Front. Phys.* **15** 14601
[66] Schäfer M B, Zelenka O, Nitz A H, Ohme F and Brügmann B 2022 Training strategies for deep learning gravitational-wave searches *Phys. Rev.* D **105** 043002
[67] Zhang J, Li Y, Xiao W and Zhang Z 2020 Non-iterative and fast deep learning: multilayer extreme learning machines *J. Franklin Inst.* **357** 8925
[68] LeCun Y, Bengio Y and Hinton G 2015 Deep learning *Nature* **521** 436–44
[69] Zhang M and Shi W 2020 A Feature difference convolutional neural network-based change detection method *IEEE Trans. Geosci. Remote Sens.* **58** 7232
[70] Zhang M, Li W and Du Q 2017 Collaborative classification of hyperspectral and visible images with convolutional neural network *J. Appl. Remote Sens.* **11** 042607
[71] Zhu Q and Zu X 2022 Fully convolutional neural network structure and its loss function for image classification *IEEE Access* **101** 35541
[72] Bai C, Huang L, Pan X, Zheng J and Chen S 2018 Optimization of deep convolutional neural network for large scale image retrieval *Neurocomputing* **303** 60
[73] Er M J, Zhang Y, Wang N and Pratama M 2016 Attention pooling-based convolutional neural network for sentence modelling *Inf. Sci.* **373** 388
[74] Lopez A and Freese K 2015 First test of high frequency Gravity Waves from inflation using Advanced LIGO *J. Cosmol. Astropart. Phys.* **2015** 037
[75] Dev P S B and Mazumdar A 2016b Probing the scale of new physics by Advanced LIGO/VIRGO *Phys. Rev.* D **93** 104001
[76] Hindmarsh M, Lüben M, Lumma J and Pauly M 2021 Phase transitions in the early universe *SciPost Phys. Lect. Notes* **24**
[77] Caprini C *et al* 2016 Science with the space-based interferometer eLISA. II: gravitational waves from

cosmological phase transitions *J. Cosmol. Astropart. Phys.* **2016** 001
[78] Cai R-G, Cao Z, Guo Z-K, Wang S-J and Yang T 2017 The gravitational-wave physics *Natl. Sci. Rev.* **4** 687
[79] Kahniashvili T, Kosowsky A, Gogoberidze G and Maravin Y 2008a Detectability of gravitational waves from phase transitions *Phys. Rev.* D **78** 043003
[80] Kahniashvili T, Campanelli L, Gogoberidze G, Maravin Y and Ratra B 2008b Gravitational radiation from primordial helical inverse cascade magnetohydrodynamic turbulence *Phys. Rev.* D **78** 123006
[81] Kahniashvili T, Kisslinger L and Stevens T 2010 Gravitational radiation generated by cosmological phase transition magnetic fields *Phys. Rev.* D **81** 023004
[82] Caprini C, Durrer R and Servant G 2009 The stochastic gravitational wave background from turbulence and magnetic fields generated by a first-order phase transition *J. Cosmol. Astropart. Phys.* **2009** 024
[83] Maggiore M 2000 Gravitational wave experiments and early universe cosmology *Phys. Rep.* **331** 283
[84] Maggiore M *et al* (LIGO Scientific, Virgo) 2021a Open data from the first and second observing runs of Advanced LIGO and Advanced Virgo *SoftwareX* **13** 100658
[85] Abbott R *et al* 2023 Open data from the third observing run of LIGO, Virgo, KAGRA, and GEO *Astrophys. J. Suppl. Ser.* **267** 29
[86] Agarap A F 2019 arXiv:1803.08375
[87] Luo L, Xiong Y and Liu Y 2019 Adaptive Gradient Methods with Dynamic Bound of Learning Rate *International Conference on Learning Representations*
[88] Kingma D P and Ba J 2017 arXiv:1412.6980
[89] Ruder S 2017 arXiv:1609.04747
[90] Christensen N 1992 Measuring the stochastic gravitational-radiation background with laser-interferometric antennas *Phys. Rev.* D **46** 5250
[91] Flanagan E E 1993 Sensitivity of the laser interferometer gravitational wave observatory to a stochastic background, and its dependence on the detector orientations *Phys. Rev.* D **48** 2389
[92] Christensen N 1997 Optimal detection strategies for measuring the stochastic gravitational radiation background with laser interferometric antennas *Phys. Rev.* D **55** 448
[93] Allen B and Romano J D 1999 Detecting a stochastic background of gravitational radiation: Signal processing strategies and sensitivities *Phys. Rev.* D **59** 102001
[94] Gasperini M and Ungarelli C 2001 Detecting a relic background of scalar waves with LIGO *Phys. Rev.* D **64** 064009
[95] Whelan J T, Anderson W G, Casquette M, Díaz M C, Heng I S, McHugh M, Romano J D, Jr C W T, Trejo R M and Vecchio A 2002 Progress on stochastic background search codes for LIGO *Class. Quantum Grav.* **19** 1521
[96] Corda C 2012 The LIGO-LIGO cross correlation for the detection of relic scalar gravitational waves *New Astron.* **17** 646
[97] Thrane E and Romano J D 2013 Sensitivity curves for searches for gravitational-wave backgrounds *Phys. Rev.* D **88** 124032
[98] Abbott B P *et al* (LIGO Scientific Collaboration and Virgo Collaboration) 2017 Upper limits on the stochastic gravitational-wave background from advanced LIGO's first observing run *Phys. Rev. Lett.* **118** 121101
[99] Abbott B P *et al* (LIGO Scientific Collaboration and Virgo Collaboration) 2018 Search for tensor, vector, and scalar polarizations in the stochastic gravitational-wave background *Phys. Rev. Lett.* **120** 201102
[100] Caprini C and Figueroa D G 2018 Cosmological backgrounds of gravitational waves *Class. Quantum Grav.* **35** 163001
[101] Christensen N 2018 Stochastic gravitational wave backgrounds *Rep. Prog. Phys.* **82** 016903
[102] Abbott B P *et al* (LIGO Scientific and Virgo Collaboration) 2019 Search for the isotropic stochastic background using data from Advanced LIGO's second observing run *Phys. Rev.* D **100** 061101
[103] Li Y, Fan X and Gou L 2019 Constraining the stochastic gravitational wave from string cosmology with current and future high-frequency detectors *Astrophys. J.* **887** 28
[104] Abbott B P *et al* (LIGO Scientific Collaboration, Virgo Collaboration, and KAGRA Collaboration) 2021b Upper limits on the isotropic gravitational-wave background from Advanced LIGO and Advanced Virgo's third observing run *Phys. Rev.* D **104** 022004
[105] Hu Y, Wang P-P, Tan Y-J and Shao C-G 2022 Full analytic expression of overlap reduction function for gravitational wave background with pulsar timing arrays *Phys. Rev.* D **106** 024005
[106] Renzini A I, Goncharov B, Jenkins A C and Meyers P M 2022 Stochastic gravitational-wave backgrounds: current detection efforts and future prospects *Galaxies* **10** 18
[107] Cai R-G, Guo Z-K, Hu B, Liu C, Lu Y, Ni W-T, Ruan W-H, Seto N, Wang G and Wu Y-L 2024 On networks of space-based gravitational-wave detectors *Fundament. Res.* **4** 1072